Research in Astronomy and Astrophysics, 24:095020 (11pp), 2024 September https://doi.org/10.1088/1674-4527/ad74df

Comparison of NH_3 and ^{12}CO, ^{13}CO, $C^{18}O$ Molecular Lines in the Aquila Rift Cloud Complex

Kadirya Tursun[1,2,3], Jarken Esimbek[1,2,3], Willem Baan[1,4], Toktarkhan Komesh[5,6], Xindi Tang[1,2,3], Gang Wu[1,2,3], Jianjun Zhou[1,2,3], Yuxin He[1,2,3], Dalei Li[1,2,3], Dongdong Zhou[1,2,3], and Yingxiu Ma[1,2,3]
[1] Xinjiang Astronomical Observatory, Chinese Academy of Sciences, Urumqi 830011, China; kadirya@xao.ac.cn, jarken@xao.ac.cn
[2] Key Laboratory of Radio Astronomy, Chinese Academy of Sciences, Urumqi 830011, China
[3] Xinjiang Key Laboratory of Radio Astrophysics, Urumqi 830011, China
[4] Netherlands Institute for Radio Astronomy, NL-7991PD Dwingeloo, The Netherlands
[5] Energetic Cosmos Laboratory, Nazarbayev University, Astana 010000, Kazakhstan
[6] Institute of Experimental and Theoretical Physics, Al-Farabi Kazakh National University, Almaty 050040, Kazakhstan
Received 2024 May 5; revised 2024 August 16; accepted 2024 August 21; published 2024 September 19

Abstract

The observations of the Aquila Rift cloud complex at 23.708 and 115.271 GHz made using the Nanshan 26 m radio telescope and the 13.7 m millimeter-wavelength telescope are presented. We find that the CO(1 − 0) gas distribution is similar to the NH_3 gas distribution in the Aquila Rift cloud complex. In some diffusion regions characterized by CO, we identified several dense clumps based on the distribution of detected ammonia molecular emission. Through the comparison of spectral line parameters for NH_3, ^{13}CO, and $C^{18}O$, our study reveals that the line center velocities of the NH_3, ^{13}CO, and $C^{18}O$ lines are comparable and positively correlated, indicating that they originate from the same emission region. No significant correlation was identified for other parameters, including integrated intensity, line widths, main beam brightness temperature, as well as the column densities of NH_3, ^{13}CO, and $C^{18}O$. The absolute difference in line-center velocities between the ^{13}CO and NH_3 lines is less than both the average line width of NH_3 and that of ^{13}CO. This suggests that there are no significant movements of NH_3 clumps in relation to their envelopes. The velocity deviation is likely due to turbulent activity within the clumps.

Key words: ISM: clouds – ISM: molecules – stars: formation

1. Introduction

The Aquila Rift cloud complex, a frequently studied and relatively nearby region, harbors a diverse collection of active star-forming regions, such as Serpens Main, Serpens South, Serpens MWC 297, and W 40. (Gutermuth et al. 2008). In this paper, we concentrate on the section of the Aquila Rift complex that contains two notable star-forming locations: Serpens South and W 40. Serpens South, situated in the western portion of the Aquila Rift cloud complex, is a notable region of star formation that hosts a young embedded stellar cluster (Gutermuth et al. 2008). The region has a filamentary structure on the cusp of a burst of low-mass star formation. W 40 is a site of ongoing high-mass star formation located further to the east in equatorial coordinates. It not only contains dense molecular cores (Dobashi et al. 2005), but also includes a blistered H II region, which is powered by a pre–main–sequence stars contained compact OB association (e.g., Zeilik & Lada 1978; Smith et al. 1985; Vallee 1987; Kuhn et al. 2010; Rodríguez et al. 2010; Mallick et al. 2013).

The whole Aquila complex has been studied by the Herschel Gould Belt Survey,[7] and provided detections of more than 500 starless cores, which were imaged in dust emission at 70–500 μm (Könyves et al. 2010). The recently measured distance to Serpens Main and W 40 is 436 pc, and the distance to Serpens South should be similar, since the two sources are connected kinematically (Ortiz-León et al. 2017, 2018). The mass of the W 40 giant molecular cloud was estimated to be $\sim 1.4 \times 10^5\, M_\odot$ by Su et al. (2020).

Comparative surveys of the CO(1 − 0) and NH_3 molecular lines in star-forming regions have been presented by Levshakov et al. (2013), Li et al. (2016), Ladeyschikov et al. (2016) and Armillotta et al. (2020). Those studies show that both CO and ^{13}CO are not only indicators of dense gas but also those of outflows and low-density regions (Levshakov et al. 2013). Furthermore, CO may exhibit saturation broadening. It is widely recognized that carbon-chain molecules are depleted from the gas phase in the central regions due to their freeze-out onto dust grains (e.g., Tafalla et al. 2004). Consequently, C-bearing molecules are typically found in the outer regions of the cores. This is the reason that CO and ^{13}CO are sub-optimal tracers for dense molecular gas. Conversely, Nitrogen-bearing molecules like ammonia are concentrated within the inner cores, where the gas density reaches approximately $10^5\,cm^{-3}$. Ammonia remains detectable in the gas phase because it is resistant to depletion onto dust grains (e.g., Bergin & Langer 1997). Generally, the

[7] http://www.herschel.fr/cea/gouldbelt/en/index.php

Table 1
Main Observation Parameters of the Nanshan and Delingha Telescopes

Parameters	Nanshan Telescope	Delingha Telescope
Telescope	Nanshan 26 m antenna	Delingha 13.7 m antenna
Receiver	*K*-band receiver	3 mm receiver
Mode	On-The-Fly	On-The-Fly
Molecular lines	NH_3 (1,1) and (2,2)	^{12}CO, ^{13}CO, $C^{18}O$
Rest frequency	23.708 GHz	115.271 GHz
Bandwidth	64 MHz	1 GHz
Channel number	8192	16384
Beam size	$\sim 2'$	$\sim 50''$
Velocity resolution	~ 0.1 km s^{-1}	~ 0.17 km s^{-1}
Main beam efficiency	59%	50%
Reference position	$l = 28.^{\circ}59$, $b = 3.^{\circ}55$	$l = 28.^{\circ}59$, $b = 3.^{\circ}55$

^{12}CO and ^{13}CO emission lines are optically thick and thin respectively, while NH_3 emission line can both be optically thick and thin. Therefore, these three lines share some common attributes while also exhibiting distinct characteristics.

Although a great number of molecular line observations have been carries out for the Aquila Rift cloud complex, such as in CO (Nakamura et al. 2017; Su et al. 2019, 2020; Komesh et al. 2020), in NH_3 (Levshakov et al. 2013, 2014; Friesen et al. 2016; Tursun et al. 2020) and in H_2CO (Komesh et al. 2019), there are no correlation studies between the NH_3 and the CO molecules. In this paper, we chose the Aquila molecular cloud to carry out correlation study between the NH_3 and the CO molecular lines.

The remainder of this paper is organized as follows: In Section 2 we describe our data and data reduction. Results are highlighted in Section 3, followed by the discussion presented in Section 4. Finally, conclusions are summarized in Section 5.

2. Observations and Data Reduction

2.1. Archival Data

The data were taken between 2017 March and 2018 August, with the Nanshan 26 m radio telescope (NSRT) located near Urumqi P. R. China. We observed the NH_3 (1,1) and (2,2) lines toward the Aquila Rift cloud complex. We used a 22.0–24.2 GHz dual polarization channel superheterodyne receiver. The main observation parameters of the Nanshan telescope and reference position are listed in Table 1.

The observations were centered on a rest frequency of 23.708 GHz to simultaneously capture the NH_3 (1,1) transition at 23.694 GHz and the (2,2) transition at 23.723 GHz. The conversion of antenna temperatures T_A^* to main beam brightness temperatures T_{MB} was achieved using a beam efficiency value of 0.59. The system temperature, as measured on the T_A^* scale, was approximately 50 K at a frequency of 23.708 GHz. The mapping was conducted using the on-the-fly (OTF) mode, utilizing a grid size of $6' \times 6'$ and a sampling interval of $30''$. Calibration of the observations was achieved by referencing periodically injected signals, occurring every 6 s, from a noise diode. IRAS 0033+636 ($\alpha = 00{:}36{:}47.51$, $\delta = 63{:}29{:}02.1$, J2000) was the subject of repeated observations (Schreyer et al. 1996), with a main beam brightness temperature T_{MB} set at 4.5 K. Obtained systematic fluctuations and dispersion of brightness temperatures are minimal (see Appendix A of Tursun et al. 2020). The standard deviation of the mean is about 10% (see Figure A1 of Tursun et al. 2020). To validate the stability of our calibrations, we had scrutinized our NH_3 data alongside earlier NH_3 data obtained with the Green Bank Telescope, as illustrated in Figure A2 of Tursun et al. (2020). The data sets acquired from G035.39 to 0.33 are in good agreement. All the observations were conducted under optimal weather conditions and at elevations higher than 20°.

The ^{12}CO, ^{13}CO, and $C^{18}O$ lines were simultaneously observed with the 13.7 m millimeter-wave telescope of the Purple Mountain Observatory in Delingha, and data were retrieved from the Millimeter Wave Radio Astronomy Database.[8] The central coordinate of the OTF observations pattern is located at $18^h30^m03^s$, $-2°02'40''$ (J2000). The half-power beamwidth (HPBW) of the observing system is approximately $50''$. The observation system features a half-power beamwidth (HPBW) of about $50''$, a velocity resolution of 0.17 km s^{-1}, and system temperature varying between 180 and 320 K. The ^{12}CO, ^{13}CO, and $C^{18}O$ data have been smoothed to the spatial resolution and the cell size of Nanshan 26 m radio telescope, which are $120''$ and $60''$, respectively. The one-sigma noise levels for these data sets are 0.50 K, 0.35 K, and 0.35 K, respectively. The main observation parameters of Delingha telescope are also listed in Table 1. Examples of their reduced and the averaged spectra lines of NH_3 (1,1), NH_3 (2,2), ^{12}CO, ^{13}CO, and $C^{18}O$ are given in Figures 1 and 2.

2.2. Data Reduction

The CLASS and GREG packages of GILDAS[9] were used for all data reduction. For NH_3, we adopted two different fitting methods: the "GAUSS" fitting and the NH_3 (1,1) fitting. To transform the widths of the hyperfine blended lines into intrinsic line widths within the NH_3 inversion spectrum (e.g., Barranco & Goodman 1998), we further processed the averaged spectra by employing the GILDAS software's integrated "NH_3 (1,1)" fitting technique, capable of simultaneously fitting all 18 hyperfine components. Through the NH_3 (1,1) fitting, we can derive the integrated intensity $\int T_{MB}\, dv$, the line center velocity V_{LSR}, the intrinsic line widths Δv for each hyperfine structure (hfs) component, and the optical depth τ. The main beam brightness temperatures (T_{MB}) are derived using the GAUSS fitting method. These methods have been previously employed in similar studies, for instance by

[8] http://www.radioast.nsdc.cn
[9] http://www.iram.fr/IRAMFR/GILDAS/

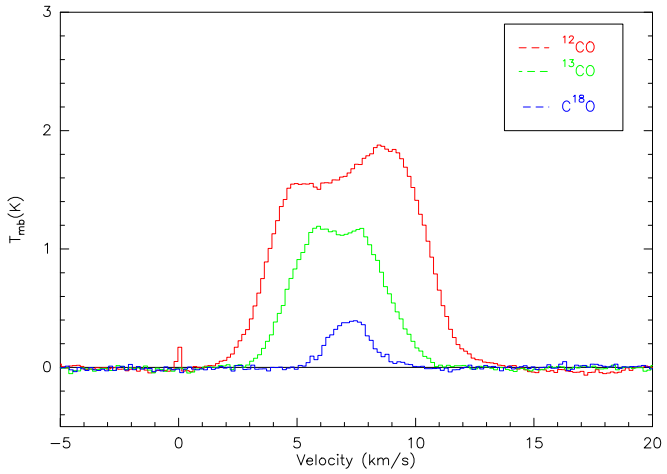

Figure 1. Averaged spectra of ^{12}CO(red), ^{13}CO(green), and C^{18}O(blue) for the Aquila Rift cloud complex. Spectra only with at least three consecutive channels $\geqslant 3\sigma$ are averaged.

Wienen et al. (2012) and Wu et al. (2018). Figure 2 displays representative examples of the reduced and fitted spectra for the NH_3 (1,1) and (2,2) inversion transitions. The spectra line parameters of the NH_3 (1,1) transition lines are given in Table 2.

Owing to the relative weakness of the hyperfine satellite lines in the NH_3 (2,2) transition, the optical depths for NH_3 (2,2) were not measured. Instead, a single Gaussian profile was utilized to fit the main group of NH_3 (2,2) hyperfine components. The spectra line parameters for the NH_3 (2,2) transition lines are detailed in Table 2.

For ^{12}CO, ^{13}CO, and C^{18}O, we applied the "GAUSS" fitting to obtain the integrated intensity, the velocity at the line center, the line width, and the main beam brightness temperatures. The spectra line parameters for the CO isotopic lines are presented in Table 2.

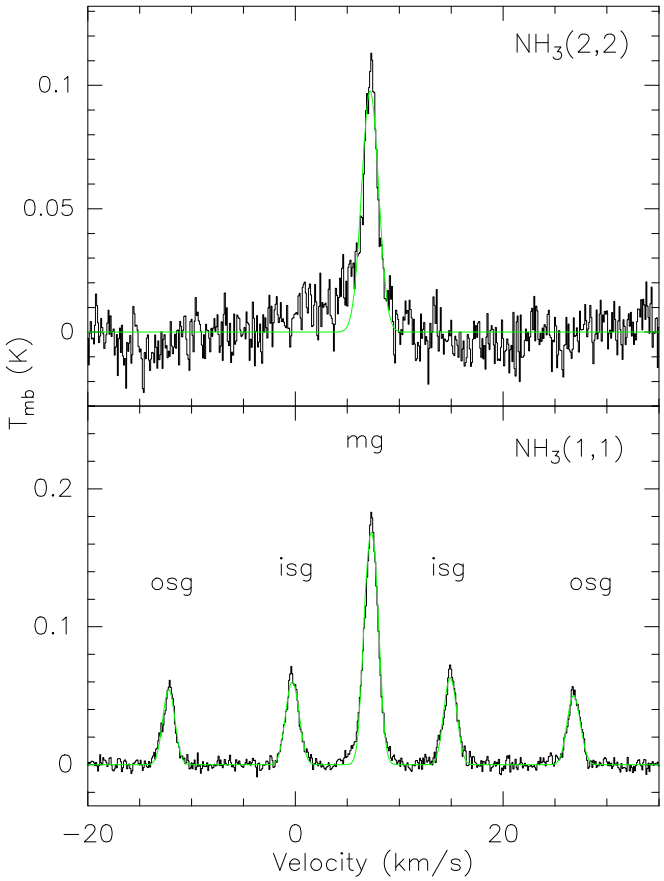

Figure 2. Averaged spectra of NH_3 (1,1) (lower panel) and NH_3 (2,2) (upper panel) for the Aquila Rift cloud complex. Spectra are averaged only if they have at least three consecutive channels with a signal-to-noise ratio of $\geqslant 3\sigma$. In each panel, the black solid line depicts the observed spectrum, while the green solid line represents the NH_3 (1,1) fitting in the lower panel and the Gaussian fitting of the NH_3 (2,2) line in the upper panel (see Section 2.2). The clusters of hyperfine components labeled "mg," "isg," and "osg" correspond to the main, inner-satellite, and outer-satellite groupings, respectively.

3. The Results

3.1. The Distribution of the CO Gas

Figure 3 displays the integrated intensity maps for the ^{12}CO, ^{13}CO, and C^{18}O lines, covering a velocity interval of $4 < V_{LSR} < 10\,km\,s^{-1}$, and allowing of which have a signal-to-noise ratio (S/N) in excess of 3. The velocity range was selected with reference to the averaged spectral velocity range of the Aquila giant molecular cloud and the actual velocity of each spectral line. It is clear from the Figure 3 that the ^{12}CO molecule has the largest distribution range and was detected in the whole dense region. The ^{13}CO molecule represents the diffused gas and can also be found in the dense part, while the C^{18}O molecule can only be identified within the most compact areas of Serpens South and W 40.

Observing the Aquila Rift morphology, it becomes evident that within the Serpens South area, there is a prominent ridge characterized by intense NH_3 (1,1) emission stretching from southwest to northeast. This ridge encompasses numerous cores and extends over a total length of approximately 15′. NH_3 emissions of lesser intensity are detected, reaching further both to the south and to the north. The NH_3 distribution exhibits a ring-shaped pattern, with its central point situated within region 4 (see Figure 1 in Tursun et al. 2020 for region 4). The feature, with a radius ranging from 25′ to 30′, or around 3.5 pc, is approximately circular. It shows significant emission of dust and NH_3.

Figure 3 illustrates that the morphology of ^{12}CO, ^{13}CO, and C^{18}O of the Aquila Rift is consistent with that of the Aquila giant molecular cloud discussed in Section 3.1 (Tursun et al. 2020),

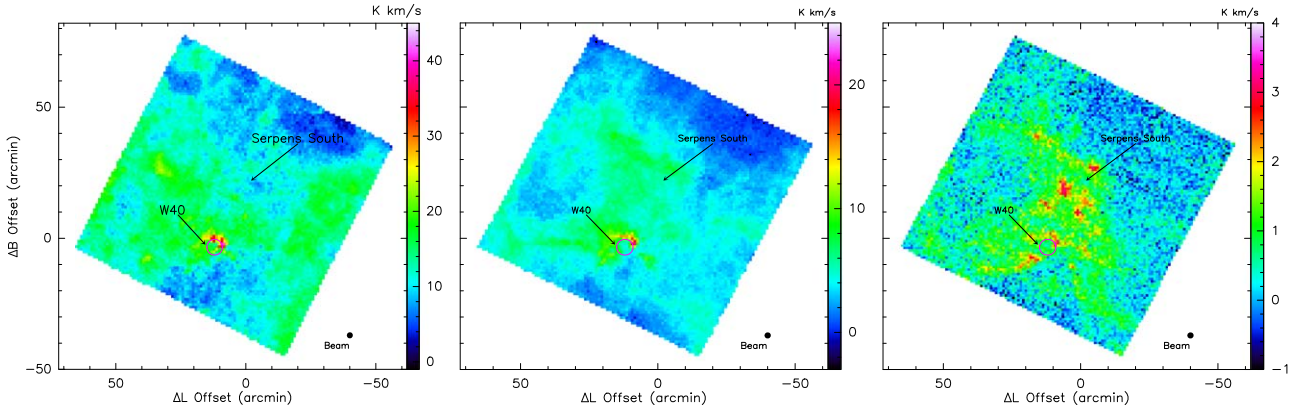

Figure 3. Integrated intensity maps of ^{12}CO (left), ^{13}CO (middle), and C^{18}O (right). The reference position is $l = 28.^{\circ}59$, $b = 3.^{\circ}55$. The unit of the color bars is K km s^{-1}. The integration range is $4 < V_{\rm LSR} < 10$ km s^{-1}. The half-power beamwidth of the observation system for the 13.7 m millimeter-wave telescope at the Purple Mountain Observatory, located in Delingha, is depicted as a black filled circle in the bottom right-hand corner of each image.

Table 2
Spectral Line Parameters Obtained from the Aquila Rift Cloud Complex (See Section 2.2)

Species	Offset	Serpens South					W 40				
	(′,′)	$\int T_{\rm MB}\,dv$ (K km s^{-1})	$V_{\rm LSR}$ (km s^{-1})	Δv (km s^{-1})	$T_{\rm MB}$ (K)	τ	$\int T_{\rm MB}\,dv$ (K km s^{-1})	$V_{\rm LSR}$ (km s^{-1})	Δv (km s^{-1})	$T_{\rm MB}$ (K)	τ
NH_3 (1,1)	(0,14)	2.03	7.35	0.63	0.86	1.84					
NH_3 (1,1)	(9,0)						0.61	4.98	1.01	0.41	0.68
NH_3 (2,2)	(0,14)	0.19	7.13	1.82	0.10						
NH_3 (2,2)	(9,0)						0.26	5.02	1.23	0.20	
^{12}CO	(0,14)	7.01	4.46	2.13	3.09						
^{12}CO	(9,0)						22.03	4.41	1.86	11.11	
^{13}CO	(0,14)	5.08	7.41	3.51	1.36	0.57					
^{13}CO	(9,0)						7.99	5.30	0.81	6.21	0.81
C^{18}O	(0,14)	1.61	7.23	1.61	0.94	0.35					
C^{18}O	(9,0)						1.71	7.02	1.02	0.72	0.10

Note. The central position is $(l, b) = (28.^{\circ}59, 3.^{\circ}55)$. Offsets are given in Galactic coordinates. Parameters are derived from NH_3 (1,1) fit to the NH_3 (1,1) emission lines and Gaussian fits to the other NH_3 (2,2), ^{12}CO, ^{13}CO, and C^{18}O spectra lines. The offsets (0′, 14′) and (9′, 0′) correspond to the Serpens South and W 40 regions, respectively. The optical depth of the NH_3 (1,1) line is determined using the "NH_3 (1,1)" fitting method described in Section 2.2. The optical depths for ^{13}CO and C^{18}O are calculated using Equations (2) and (3) provided in Section 3.6, respectively.

and is in a ring-like structure like the Herschel color infrared image.

3.2. Comparison on Distributions of the NH_3 and CO Gas

The composite maps of the integrated intensity of the NH_3 (1,1) and (2,2) lines with the ^{12}CO, ^{13}CO, and C^{18}O molecular lines are shown in Figures 4, and 5, respectively. The color images present the integrated intensity distributions of ^{12}CO, ^{13}CO, and C^{18}O lines, and the contours indicate the integrated intensities of the NH_3 (1,1) and (2,2) lines. The reference position is $l = 28.^{\circ}59$, $b = 3.^{\circ}55$. The integration range of NH_3 (1,1) and (2,2) lines are also $4 < V_{\rm LSR} < 10$ km s^{-1}. Contours begin at a level of 0.13 K km s^{-1} (3σ) on the main beam brightness temperature scale, and increase in increments of 0.13 K km s^{-1} (see Figures 4, 5).

NH_3 (1,1) exhibits an extended distribution, and clearly traces the dense molecular gas, which includes Serpens South and W 40 (see Figure 4). NH_3 (2,2) is only detected within the most compact areas of Serpens South and W 40, and exhibits a more limited distribution (see Figure 5). The maps show that the distribution of the NH_3 gas is similar to the CO gas. In some CO molecular clouds, several dense clumps can be found by using NH_3 (1,1), as shown in the south and east regions in Figure 4.

The comparison of integrated intensities of NH_3 (1,1) lines with the ^{12}CO, ^{13}CO, and C^{18}O lines in the Aquila Rift cloud complex is shown in Figure 6. It shows that the integrated intensities of NH_3 (1,1) lines was not significantly correlated

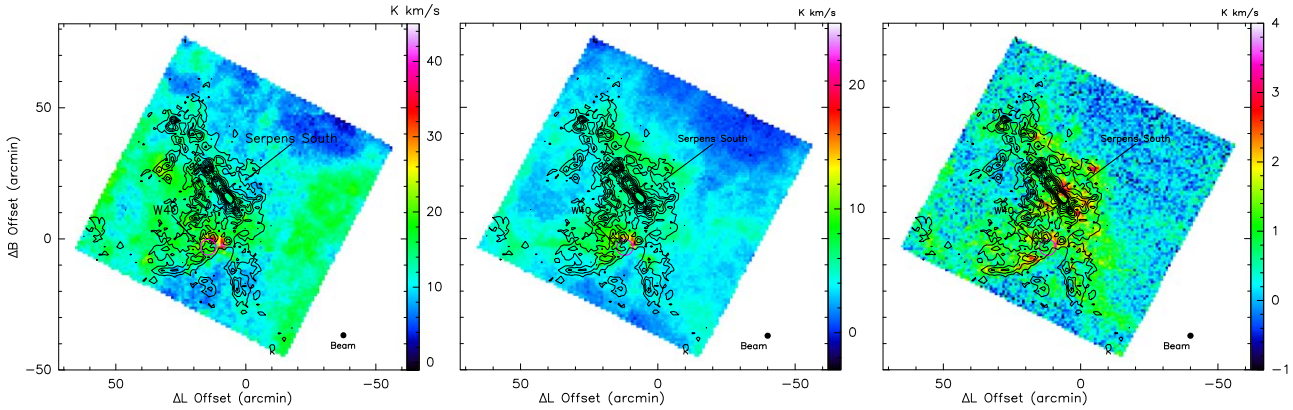

Figure 4. The composite maps of integrated intensity of colored ^{12}CO (left) with the contour lines NH_3 (1,1), colored ^{13}CO (middle) with the contour lines NH_3 (1,1), and colored $C^{18}O$ (right) with the contour lines NH_3 (1,1) in the Aquila Rift cloud complex. The black filled circles on the lower right are the same as Figure 3.

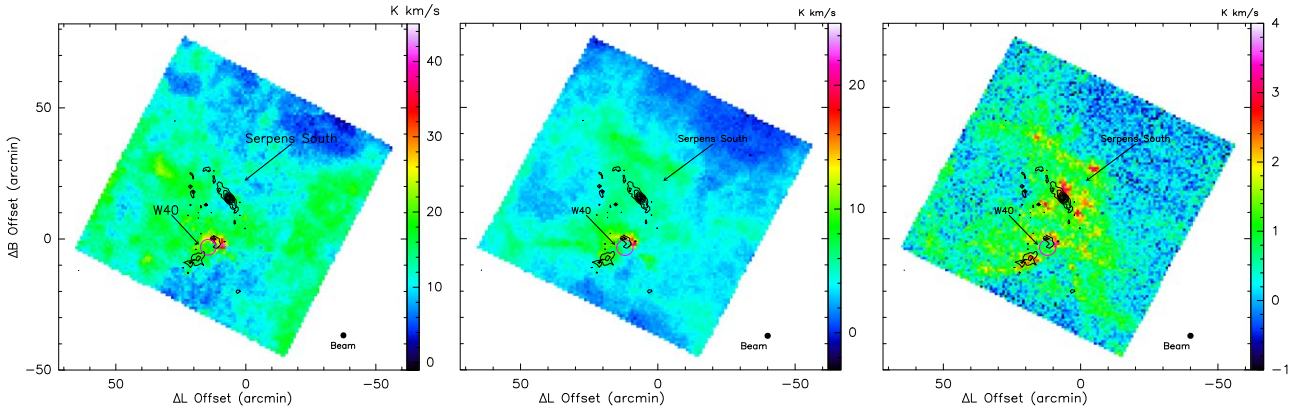

Figure 5. Same as Figure 4, but contour lines are for the NH_3 (2,2).

with the integrated intensities of ^{13}CO and $C^{18}O$ lines. Furthermore, the correlation between the integrated intensities of the NH_3 (1,1) lines and the $C^{18}O$ lines is stronger than that between the NH_3 (1,1) lines and the ^{12}CO or ^{13}CO lines (see Figures 4, 5 and 6).

3.3. The Velocity Distributions of the NH_3 and CO Molecules

Figure 7 right panel shows that distributions of measured line center velocity for NH_3 (1,1), ^{13}CO, and $C^{18}O$. The velocity range, peak value, average value, and standard deviation for the NH_3, ^{13}CO, and $C^{18}O$ lines are as follows, respectively: NH_3: 4.53–9.69 km s^{-1}, peak value of ∼7.00 km s^{-1}, average value of 6.99 km s^{-1}, and standard deviation of 0.76 km s^{-1}; ^{13}CO: 4.69–8.22 km s^{-1}, peak value of ∼7.00 km s^{-1}, average value of 6.94 km s^{-1}, and standard deviation of 0.73 km s^{-1}; $C^{18}O$: 6.09–9.80 km s^{-1}, peak value of ∼7.00 km s^{-1}, average value of 7.42 km s^{-1}, and standard deviation of 1.47 km s^{-1}. While the peak velocity values of the NH_3, ^{13}CO, and $C^{18}O$ lines are identical, and the average velocity values of NH_3 and ^{13}CO are nearly the same.

The line center velocities of NH_3 (1,1) was plotted against with those of ^{13}CO, $C^{18}O$ lines in Figure 7 left panel. It can be found that the correlations in velocity between the NH_3 (1,1)– ^{13}CO and NH_3 (1,1)– $C^{18}O$ lines are significant, with a linear correlation coefficient (r) of 0.51 and 0.49, respectively. The solid red and green lines provide the linear fit for NH_3 (1,1)– ^{13}CO and NH_3 (1,1)– $C^{18}O$, respectively. The blue dashed line indicates the same central velocity for both the CO and NH_3 lines. We mapped the Aquila Rift cloud complex for the NH_3, ^{12}CO, ^{13}CO and $C^{18}O$ (Figures 3, 4 and 5). The mappings reveal a consistent distribution of NH_3, ^{12}CO, ^{13}CO, and $C^{18}O$ on a scale of ∼12 pc. The velocity correlation diagram for the Aquila Rift cloud complex (Figure 7) also indicates that the line center velocities of these lines are comparable and positively correlated, suggesting that they originate from the same emission region.

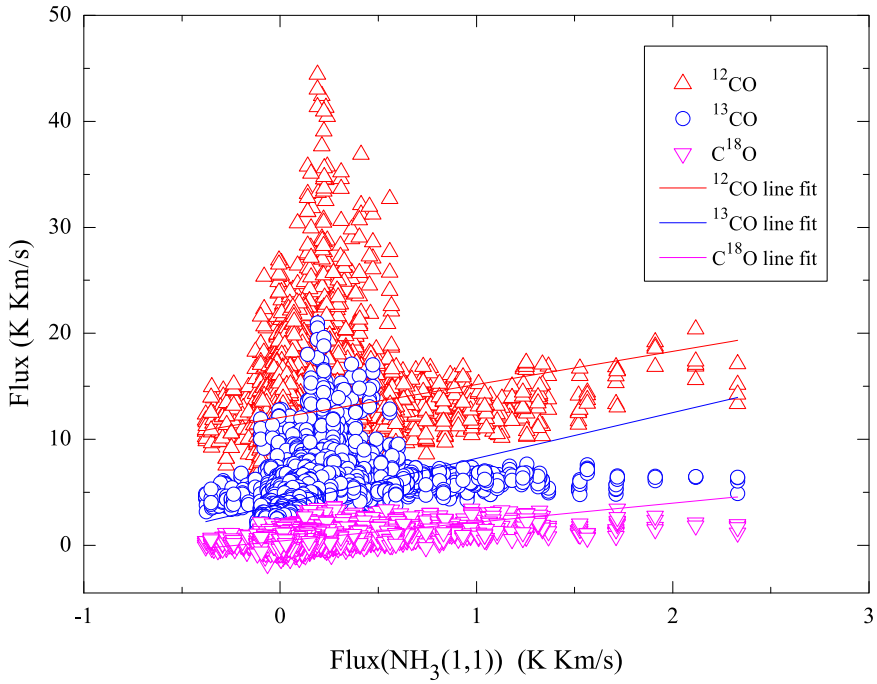

Figure 6. Correlation between the integrated intensity of NH_3 (1,1) line and ^{12}CO, ^{13}CO, $C^{18}O$ lines, respectively. The solid red, blue, and purple lines are the linear fits for NH_3 (1,1) with ^{12}CO, NH_3 (1,1) with ^{13}CO, and the NH_3 (1,1) with $C^{18}O$ data, respectively.

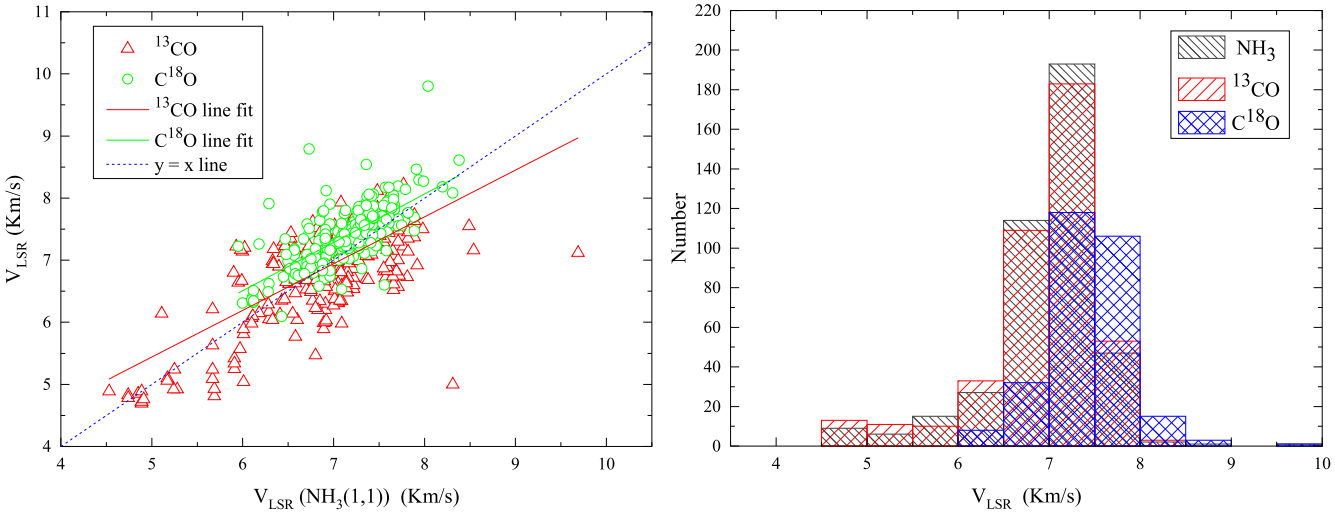

Figure 7. Left: Correlation between the line center velocities of NH_3 (1,1) and ^{13}CO, $C^{18}O$ lines at corresponding points in the Aquila Rift cloud complex. The solid red, and green lines are linear fits for NH_3 (1,1) with ^{13}CO data, and the NH_3 (1,1) with $C^{18}O$ data, respectively. The blue dashed line shows the identical line center velocity of CO and NH_3 lines. Right: Histograms showing the distributions of measured line center velocity for NH_3 (1,1), ^{13}CO, and $C^{18}O$.

3.4. The Line width Distributions of the NH_3 and CO Molecules

The right panel of Figure 8 presents the distribution of observed line widths for the NH_3 (1,1) transition, as well as for the ^{13}CO and $C^{18}O$ isotopologues. For NH_3, ^{13}CO, and $C^{18}O$ lines, the respective parameters are as follows: NH_3 has a line width range of 0.10–5.09 km s^{-1} with a peak value of ∼1.00 km s^{-1}, an average value of 1.42 km s^{-1}, and a standard deviation of 2.52 km s^{-1}; ^{13}CO spans a line width range of 1.10–5.61 km s^{-1} with a peak value of ∼3.00 km s^{-1}, an average value of 3.24 km s^{-1}, and a standard deviation of 1.46 km s^{-1}; $C^{18}O$ is characterized by a line width range of

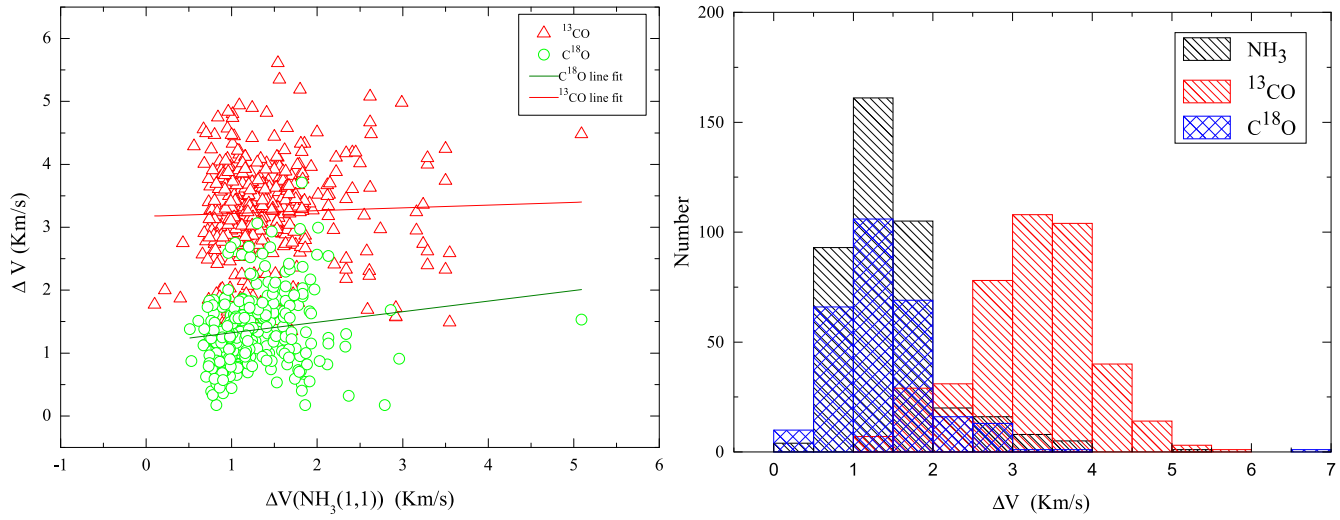

Figure 8. Left: Correlation between the NH_3 (1,1) line widths and the ^{13}CO, $C^{18}O$ line widths at corresponding points in the Aquila Rift cloud complex. The solid red, and green lines are linear fits for NH_3 (1,1) with the ^{13}CO data, and the $C^{18}O$ data, respectively. Right: A histogram showing the measured line widths for NH_3 (1,1), ^{13}CO, and $C^{18}O$.

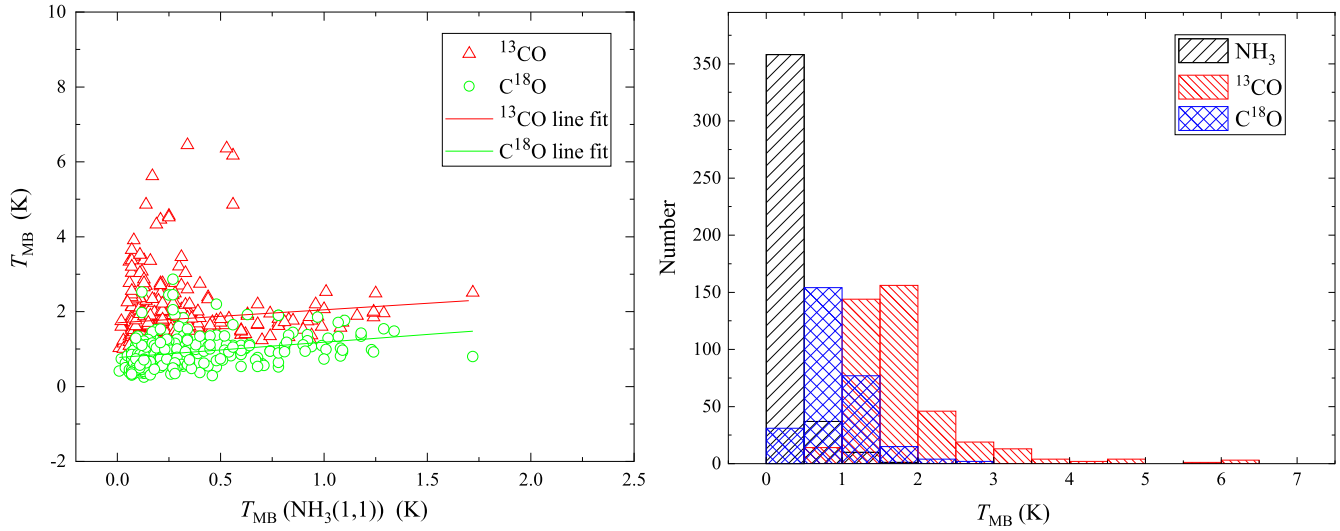

Figure 9. Left: The correlation between the main beam brightness temperatures of NH_3 (1,1) and the ^{13}CO, $C^{18}O$ at corresponding points in the Aquila Rift cloud complex. The solid red, and green lines are linear fits for NH_3 (1,1) with the ^{13}CO data, and the $C^{18}O$ data, respectively. Right: A histogram showing the measured main beam brightness temperatures for NH_3 (1,1), ^{13}CO, and $C^{18}O$.

0.17–6.78 km s^{-1}, a peak value of ∼1.00 km s^{-1}, an average value of 1.37 km s^{-1}, and a standard deviation of 0.28 km s^{-1}. The peak values and average line widths of the NH_3 and $C^{18}O$ lines are similar to each other, whereas the ^{13}CO lines exhibit higher peak values and broader average line widths.

Figure 8 left panel displays a comparison of the line widths for NH_3 (1,1) with those of ^{13}CO and $C^{18}O$. The plot reveals that there is no significant correlation between the line widths of NH_3 and the line widths of ^{13}CO and $C^{18}O$.

3.5. The Main Beam Brightness Temperature Distributions of the NH_3 and CO Molecules

Figure 9 right panel shows that distributions of measured main beam brightness temperature for NH_3 (1,1), ^{13}CO, and $C^{18}O$. The parameters for the NH_3, ^{13}CO, and $C^{18}O$ lines are detailed below: For NH_3, the T_{MB} range extends from 0.01 to 1.72 K, peaking at ∼0.02 K, with an average of 0.25 K and a standard deviation of 0.04 K. ^{13}CO exhibits a T_{MB} range from

0.70 to 6.45 K, reaching a peak at ∼1.50 K, with an average of 1.79 K and a standard deviation of 1.08 K. $C^{18}O$ is identified by a T_{MB} range of 0.25–2.86 K, a peak value of ∼0.50 K, an average of 0.91 K, and a standard deviation of 0.06 K.

A comparison of main beam brightness temperatures of NH_3 (1,1) with ^{13}CO, $C^{18}O$ lines is shown in Figure 9 left panel. It is evident that there is no significant correlation between the main beam brightness temperatures of the NH_3 (1,1) line and those of ^{13}CO and $C^{18}O$.

3.6. Comparison of the NH_3 and CO Column Densities

For this investigation, the characteristics of the molecular gas have been analyzed based on the condition that the entire molecular gas sample is in a state of local thermodynamic equilibrium (LTE). We are postulating that the ^{12}CO emission is characterized by optical thickness, and we are further consider a beam-filling factor of unity. Given this, we can calculate the excitation temperature (T_{ex}) as follows (Pineda et al. 2010; Kong et al. 2015; Lin et al. 2016):

$$T_{ex} = \frac{h\nu_{^{12}CO}}{k}\left[\ln\left(1+\frac{h\nu_{^{12}CO}/k}{T_{mb,^{12}CO}+J_\nu(T_{bg})}\right)\right]^{-1}\ \mathrm{K}$$
$$= 5.53\left[\ln\left(1+\frac{5.53}{T_{mb,^{12}CO}+0.818}\right)\right]^{-1}\ \mathrm{K}, \quad (1)$$

where $T_{mb,^{12}CO}$ represents the maximum main-beam temperature of the ^{12}CO transition in units of K. The effective radiation temperature is defined by Ulich & Haas (1976), which is $J_\nu(T) = \frac{h\nu/k}{\exp(h\nu/(kT))-1}$, and the temperature of the cosmic microwave background radiation is $T_{bg} = 2.7$ K. The excitation temperature ranges from 3.9 to 13.0 K in the whole observed region. Assuming that different isotopologues have the same T_{ex}, the optical depths of ^{13}CO (τ_{13}), $C^{18}O$ (τ_{18}), and the column densities of ^{13}CO ($N(^{13}CO)$), $C^{18}O$ ($N(C^{18}O)$) were estimated as follows (Lada et al. 1994; Kawamura et al. 1998; Lin et al. 2016):

$$\tau(C^{18}O) = -\ln\left[1-\frac{T_{mb,C^{18}O}}{5.27[J_1(T_{ex})-0.166]}\right], \quad (2)$$

$$\tau(^{13}CO) = -\ln\left[1-\frac{T_{mb,^{13}CO}}{5.29[J_2(T_{ex})-0.164]}\right], \quad (3)$$

and

$$N(C^{18}O) = 2.42\times10^{14}\frac{\tau(C^{18}O)\Delta V(C^{18}O)T_{ex}}{1-\exp(-5.27/T_{ex})}, \quad (4)$$

$$N(^{13}CO) = 2.42\times10^{14}\frac{\tau(^{13}CO)\Delta V(^{13}CO)T_{ex}}{1-\exp(-5.29/T_{ex})}, \quad (5)$$

where $J_1(T_{ex}) = 1/[\exp(5.27/T_{ex})-1]$, $J_2(T_{ex}) = 1/[\exp(5.29/T_{ex})-1]$, and ΔV is the FWHM in km s^{-1}.

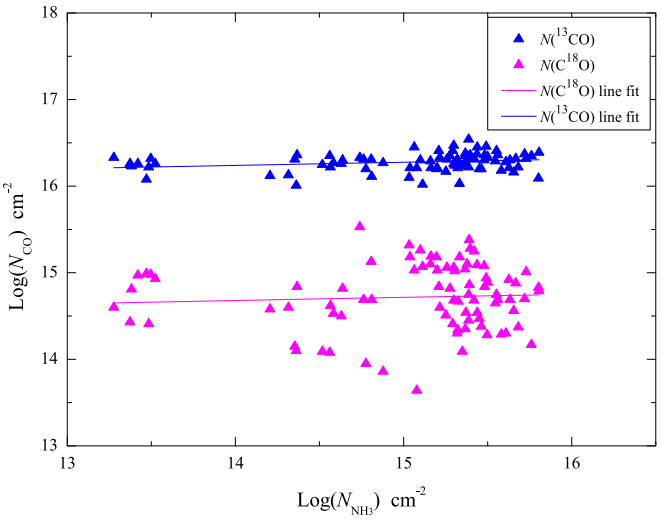

Figure 10. Correlation between the NH_3 (1,1) and the ^{13}CO, and $C^{18}O$ column densities at corresponding points in the Aquila Rift cloud complex. The solid blue, and purple lines are linear fits for NH_3 (1,1) with the ^{13}CO data, and the $C^{18}O$ data, respectively.

The optical depth of $C^{18}O$ calculated by the above formula is between 0.1 and 3.4, with an average of 0.4 ± 0.2. The optical depth of ^{13}CO ranges from 0.2 to 4.7, with an average of 3.8 ± 0.1. The column density of $C^{18}O$ ranges from 1.2×10^{13} to 9.7×10^{15} cm^{-2}, with an average of 9.8 (±1.6) $\times10^{14}$ cm^{-2}, while that of ^{13}CO ranges from 9.4×10^{15} to 3.4×10^{16} cm^{-2}, with an average of 2.1 (±1.3) $\times10^{16}$ cm^{-2}. The determined ranges for the column densities of ^{13}CO and $C^{18}O$ are in agreement with those reported by Komesh et al. (2020) for the dense interstellar clouds in the Aquila region.

The column density of NH_3 (1,1) was calculated from our NH_3 observation data, using the calculation method in Tursun et al. (2020). The results show that the column density of NH_3 in the Aquila region varies from 0.2×10^{14} to 6.4×10^{15} cm^{-2}, with an average measured at 2.1 (±1.6) $\times10^{15}$ cm^{-2}. The measured NH_3 column densities for the Aquila region are in agreement with those reported for other Gould Belt star-forming regions (Friesen et al. 2017), and exhibit a range for the logarithm of the para-NH_3 column density (log N(para-NH_3)) between 13.0 and 15.5. In Serpens South, the NH_3 column density varies from 0.3×10^{14} to 6.4×10^{15} cm^{-2}, with an average of 2.6(±1.4) $\times10^{15}$ cm^{-2}, whereas in W40 the NH_3 column density ranges from 0.2 to 7.6×10^{14} cm^{-2}, with an average of 2.6 (±2.1) $\times10^{14}$ cm^{-2}.

The column density of NH_3 (1,1) was plotted against the ^{13}CO and $C^{18}O$ lines in Figure 10. It shows that the column density of NH_3 (1,1) is similar to that of $C^{18}O$, which is about two orders less than that of ^{13}CO. No significant correlation could be found between the column density of NH_3 and ^{13}CO, $C^{18}O$.

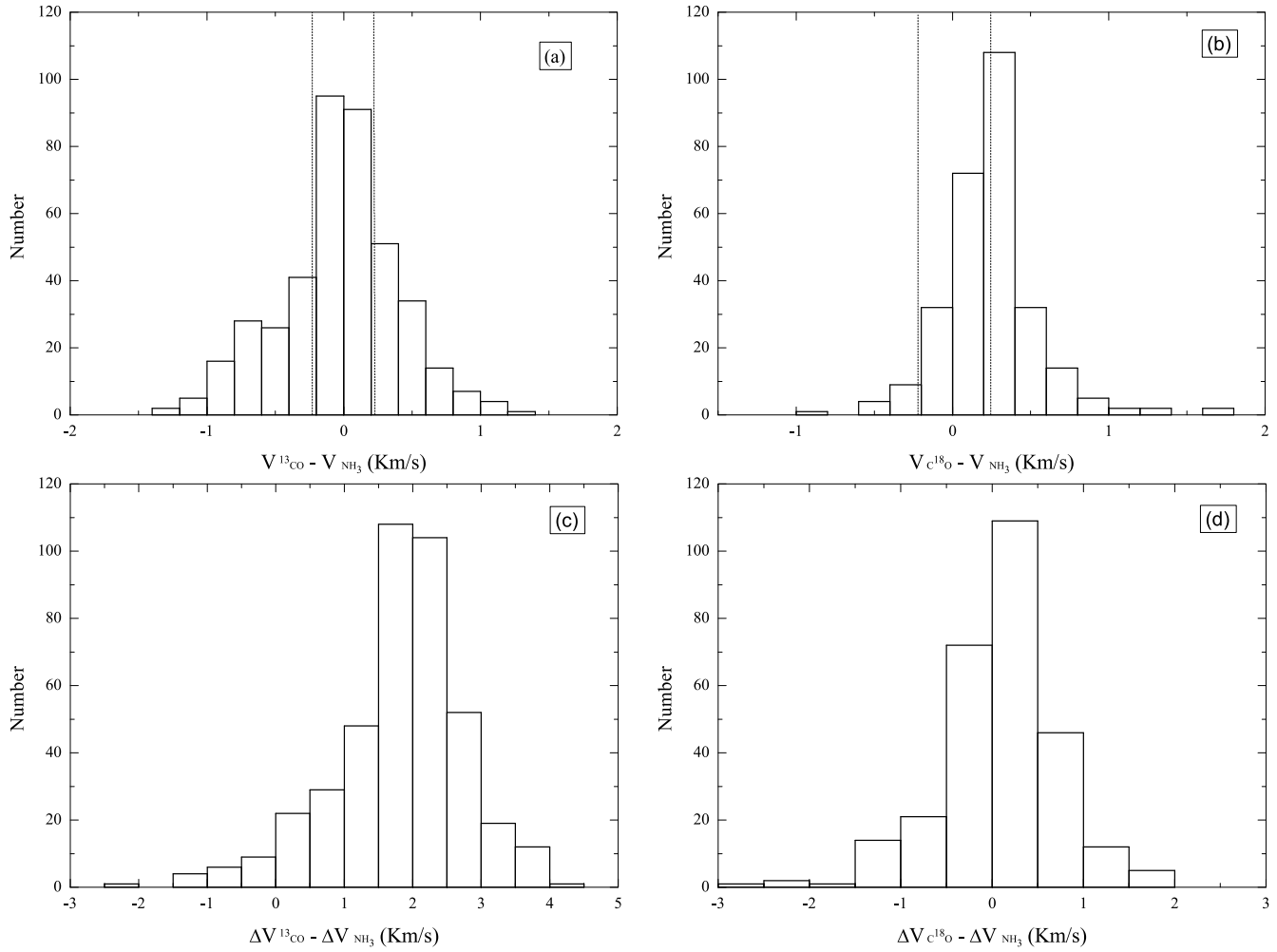

Figure 11. The distributions of the discrepancies in line-center velocities (a for ^{13}CO and NH_3, and b for $C^{18}O$ and NH_3) and in line widths (c for ^{13}CO and NH_3, and b for $C^{18}O$ and NH_3) are presented. Dotted lines in panels ((a), (b)) represent the average sound speed.

4. Discussion

We plot the absolute value of the difference between ^{13}CO and $C^{18}O$ and the NH_3 line-center velocities from Gaussian fits in Figures 11(a), (b). The average discrepancy between the central velocities of ^{13}CO and NH_3 is $0.04 \pm 0.43\,\mathrm{km\,s^{-1}}$, whereas the average velocity difference between $C^{18}O$ and NH_3 is $0.24 \pm 0.30\,\mathrm{km\,s^{-1}}$. The variations in line-center velocities of ^{13}CO and NH_3 can be compared to the sound speed, which is $0.23\,\mathrm{km\,s^{-1}}$ (for the calculation of the sound speed see Tursun et al. 2020 in Section 4.3). The majority of clumps exhibit velocity differences that exceed the sound speed, with only 28% displaying subsonic motion. Figures 11(c), (d) presents the variations in line width discrepancies between the ^{13}CO and $C^{18}O$ lines relative to NH_3. The average value of the intrinsic line widths difference among the ^{13}CO and NH_3, and $C^{18}O$ and NH_3 is $1.80 \pm 0.91\,\mathrm{km\,s^{-1}}$, and $0.07 \pm 0.67\,\mathrm{km\,s^{-1}}$, respectively.

The absolute value of the discrepancy between the ^{13}CO and NH_3 (1,1) line-center velocities is illustrated in Figure 12 as a function of the NH_3 (1,1) linewidth. If there are significant movements of NH_3 clumps relative to their envelopes, the differences in line-center velocities should be on the order of the ^{13}CO linewidths (Walsh et al. 2004). In Figure 12, the dashed red line, positioned at $1.42\,\mathrm{km\,s^{-1}}$, denotes the average linewidths of NH_3 (1,1), while the solid green line at $3.24\,\mathrm{km\,s^{-1}}$ represents the average ^{13}CO linewidths. The dashed black line in the figure shows the rms of the absolute value of the velocity difference between ^{13}CO and NH_3 (1,1). All points are below both the average linewidth of NH_3 and the average linewidth of ^{13}CO, it suggests that there are not significant movements of NH_3 clumps relative to their envelopes (as introduced before, Walsh et al. 2004). The velocity variations are presumably due to turbulent activity within the clumps. Consequently, the small relative velocities

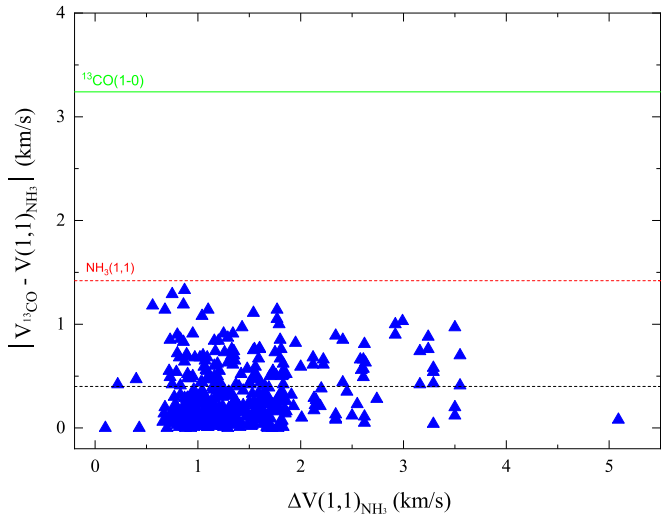

Figure 12. The plot displays the absolute difference in line-center velocities between the ^{13}CO and NH_3 (1,1) lines observed in the Aquila molecular cloud as a function of the ammonia linewidth. The dashed red line represents the average linewidths of NH_3 (1,1) lines, while the solid green line depicts the average linewidths of ^{13}CO. The dashed black line indicates the root average square (rms) of the absolute velocity differences between ^{13}CO and NH_3 (1,1) lines.

between the NH_3 clumps and the ^{13}CO clouds impose stringent constraints on the role of turbulence in the formation of these clumps.

5. Summary

We present the Nanshan 26 m telescope and the Delingha 13.7 m millimeter-wavelength telescope observations toward the Aquila Rift cloud complex. The distributions of NH_3, and ^{12}CO, ^{13}CO, C^{18}O were compared. Their spectra line parameters and derived physical parameters were also analyzed. The main results are summarized as follows:

1. The CO gas distribution is similar to the NH_3 gas distribution in the Aquila Rift cloud complex.
2. In some diffusion regions characterized by CO, we found several dense clumps, according to the distribution of detected ammonia molecular emission.
3. We compared the integrated intensity, line center velocity, line width, main beam brightness temperature, and the column density of NH_3, ^{13}CO, and C^{18}O. Our results show that the line center velocities of the three NH_3, ^{13}CO, and C^{18}O lines are comparable and positive correlated, which should demonstrate that they originate from the same emission regions. No significant correlation was found on other parameters between NH_3 and ^{13}CO, C^{18}O lines.
4. The absolute difference in line-center velocities between the ^{13}CO and NH_3 lines is smaller than the average linewidth of NH_3 and the average linewidth of ^{13}CO. It suggests that there is no significant movements of NH_3 clumps relative to their envelopes. The velocity deviation should come from turbulent activity in clumps.

Acknowledgments

We like to thank the anonymous referee for the useful suggestions that improved this study. This study relies on observations conducted using the Nanshan 26 m radio telescope, which is managed by the Key Laboratory of Radio Astronomy, the Chinese Academy of Sciences. We extend our thanks to the personnel of the Nanshan 26 m radio telescope for their support throughout the observation period. We also wish to express our gratitude to the staff of the Qinghai Radio Observing Station in Delingha for their contributions to the acquisition of the data. This work is supported by the National Key R&D Programs of China (Nos. 2023YFA1608002, and 2022YFA1603103), the regional Collaborative Innovation Project of Xinjiang Uyghur Autonomous Region (No. 2022E01050), the Tianshan Talent Program of Xinjiang Uyghur Autonomous Region (No. 2022TSYCLJ0005), the Tianchi Talent Project of Xinjiang Uyghur Autonomous Region, the Natural Science Foundation of Xinjiang Uyghur Autonomous Region (No. 2022D01E06), the Chinese Academy of Sciences (CAS) "Light of West China" Program (Nos. xbzg-zdsys-202212, 2020-XBQNXZ-017, and 2021-XBQNXZ-028), the National Natural Science Foundation of China (Nos. 12173075, 11973076, and 12103082), the Xinjiang Key Laboratory of Radio Astrophysics (No.2022D04033), the Chinese Academy of Sciences President's International Fellowship Initiative (Nos. 2022VMA0019, and 2023VMA0030), and the Science Committee of the Ministry of Science and Higher Education of the Republic of Kazakhstan (No. AP13067768). This research made use of NASA's Astrophysical Data System (ADS) to access and retrieve relevant scholarly articles and data.

ORCID iDs

Willem Baan https://orcid.org/0000-0003-3389-6838

References

Armillotta, L., Krumholz, M. R., & Di Teodoro, E. M. 2020, MNRAS, 493, 5273
Barranco, J. A., & Goodman, A. A. 1998, ApJ, 504, 207
Bergin, E. A., & Langer, W. D. 1997, ApJ, 486, 316
Dobashi, K., Uehara, H., Kandori, R., et al. 2005, PASJ, 57, S1
Friesen, R. K., Bourke, T. L., Di Francesco, J., Gutermuth, R., & Myers, P. C. 2016, ApJ, 833, 204
Friesen, R. K., Pineda, J. E.co-PIs, et al. 2017, ApJ, 843, 63
Gutermuth, R. A., Bourke, T. L., Allen, L. E., et al. 2008, ApJL, 673, L151
Kawamura, A., Onishi, T., Yonekura, Y., et al. 1998, ApJS, 117, 387
Komesh, T., Baan, W., Esimbek, J., et al. 2020, A&A, 644, A46
Komesh, T., Esimbek, J., Baan, W., et al. 2019, ApJ, 874, 172
Kong, S., Lada, C. J., Lada, E. A., et al. 2015, ApJ, 805, 58
Könyves, V., André, P., Men'shchikov, A., et al. 2010, A&A, 518, L106

Kuhn, M. A., Getman, K. V., Feigelson, E. D., et al. 2010, ApJ, 725 2485
Lada, C. J., Lada, E. A., Clemens, D. P., & Bally, J. 1994, ApJ, 429, 694
Ladeyschikov, D. A., Kirsanova, M. S., Tsivilev, A. P., & Sobolev, A. M. 2016, AstBu, 71, 208
Levshakov, S. A., Henkel, C., Reimers, D., & Wang, M. 2014, A&A, 567, A78
Levshakov, S. A., Henkel, C., Reimers, D., et al. 2013, A&A, 553, A58
Li, F. C., Xu, Y., Wu, Y. W., et al. 2016, AJ, 152, 92
Lin, S.-J., Shimajiri, Y., Hara, C., et al. 2016, ApJ, 826, 193
Mallick, K. K., Kumar, M. S. N., Ojha, D. K., et al. 2013, ApJ, 779, 113
Nakamura, F., Dobashi, K., Shimoikura, T., Tanaka, T., & Onishi, T. 2017, ApJ, 837, 154
Ortiz-León, G. N., Dzib, S. A., Kounkel, M. A., et al. 2017, ApJ, 834, 143
Ortiz-León, G. N., Loinard, L., Dzib, S. A., et al. 2018, ApJL, 869, L33
Pineda, J. L., Goldsmith, P. F., Chapman, N., et al. 2010, ApJ, 721, 686
Rodríguez, L. F., Rodney, S. A., & Reipurth, B. 2010, AJ, 140, 968
Schreyer, K., Henning, T., Koempe, C., & Harjunpaeae, P. 1996, A&A, 306, 267
Smith, J., Bentley, A., Castelaz, M., et al. 1985, ApJ, 291, 571
Su, Y., Yang, J., Yan, Q.-Z., et al. 2020, ApJ, 893, 91
Su, Y., Yang, J., Zhang, S., et al. 2019, ApJS, 240, 9
Tafalla, M., Myers, P. C., Caselli, P., & Walmsley, C. M. 2004, A&A, 416, 191
Tursun, K., Esimbek, J., Henkel, C., et al. 2020, A&A, 643, A178
Ulich, B. L., & Haas, R. W. 1976, ApJS, 30, 247
Vallee, J. P. 1987, A&A, 178, 237
Walsh, A. J., Myers, P. C., & Burton, M. G. 2004, ApJ, 614, 194
Wienen, M., Wyrowski, F., Schuller, F., et al. 2012, A&A, 544, A146
Wu, G., Qiu, K., Esimbek, J., et al. 2018, A&A, 616, A111
Zeilik, M. I., & Lada, C. J. 1978, ApJ, 222, 896